Boundary effects in DEM simulations of ballast under cyclic simple shear

Andrea Jara[1*], *Katia* Boschi[2], *Luca* Flessati[1], and *Cristina* Jommi[1,2]

[1] Department of Geoscience and Engineering, Delft University of Technology, Delft, The Netherlands
[2] Department of Civil and Environmental Engineering, Politecnico di Milano, Milano, Italy

Abstract. Ballast is a key component of railway infrastructure, and its mechanical response can be assessed through laboratory testing to support construction and maintenance strategies. Due to the large particle size and the dependence on boundary measurements to characterise the mechanical behaviour of the ballast, the influence of boundary conditions on test results is critical. This study investigates the influence of the number of particles in contact with the top loading cap on the response of ballast subjected to cyclic simple shear using DEM. The initial contact condition is systematically varied to assess its effect on macroscopic behaviour and micromechanical evolution of the sample. Results show that the number of top boundary contacts strongly affects the macroscopic response during the first loading cycles. However, these differences progressively diminish with cycling, and samples with more than 50% of the maximum achievable contacts exhibit comparable macroscopic behaviour. At the micromechanical level, the coordination number in the central and bottom regions is largely unaffected by the top boundary condition. Furthermore, the top boundary effect primarily influences the strong normal force network, while the weak network remains largely isotropic. Finally, bulk force anisotropy is higher and less reversible than bulk fabric anisotropy. These findings highlight the importance of carefully performing the sample preparation, as it strongly influences the boundary conditions, therefore, the interpretation of laboratory measurements.

1 Introduction

Railways are a strategic asset in many countries, including the Netherlands. Ageing of the infrastructure over time increases both failure risk and maintenance costs, which can be mitigated through careful maintenance management. Ballast is a key component of the railway system, as it restrains the sleepers and largely dampens the vibrations induced by passing trains before they reach the subsoil [1]. To assess the effects of ballast degradation on railway performance and to support construction and maintenance strategies, experimental tests can be conducted both in the field and in the laboratory.

Laboratory tests have been performed in the past to investigate (i) the monotonic stress-strain behaviour of clay-fouled ballast and the dynamic properties of lightweight foamed glass in triaxial tests [2, 3], (ii) the deformation properties of ballast with waste tired-derived aggregates, the cyclic behaviour of sand-gravel mixtures in cyclic simple shear tests [4, 5], and (iii) the strength and deformation characteristics of fouled and recycled ballast in direct shear tests [6].

Due to the large particle size of ballast, investigating its mechanical behaviour in the laboratory requires large-scale testing setups. However, the dimensions of such devices are typically limited to a maximum of 0.8 m in length, and 0.6 m in height [4]. As a result, it is difficult to create representative samples in the laboratory. One key challenge is ensuring proper transfer of the load from the top cap to the sample, since the particles are large compared to the contact area.

The difficulty increases further when the particles of the sample are highly angular or when the relatively low in-situ stress must be reproduced. Indeed, railway ballast is subjected to confining stresses as low as 10 kPa in the field track and is commonly tested under maximum confining stresses of about 70 kPa [7].

When ballast is tested in the laboratory, the way in which the forces are transferred to the sample plays a critical role, as stresses and strains, assumed to be representative for the whole sample, are typically inferred from measurements at the specimen boundaries. However, tracking boundary effects during testing would require placing local sensors inside the sample without disturbing it, which is virtually infeasible. In this context, numerical modelling using the discrete element method (DEM) provides a valuable complementary tool for data analysis and interpretation. With DEM simulations, quantities at the particle scale are computed, allowing for a detailed analysis of micromechanical responses under different boundary conditions.

This paper presents the results of cyclic simple shear simulations performed on virtual samples of ballast, in which the number of particles in contact with the top loading cap is varied. The aim of the analysis is to assess the influence of this boundary condition on the response

* Corresponding author: a.jarabarrera@tudelft.nl

of the sample at the macroscopic scale (i.e. inferred from external load and displacement measurements) and on the micromechanical state of the sample. The final scope of the work is to provide insights into the role of sample preparation techniques at both numerical and experimental levels.

2 Setup and sample preparation

The large-scale simple shear setup at the Slovenian Civil Engineering Institute [4] was reproduced using the open-source software Yade [8]. The setup consists of (i) a laminar box 400 mm in length and 400 mm in width, with frames 30 mm thick, and (ii) top and bottom walls (Fig. 1). In the numerical model, the laminar box frames and the top and bottom plates were represented as rigid, non-deformable boundaries.

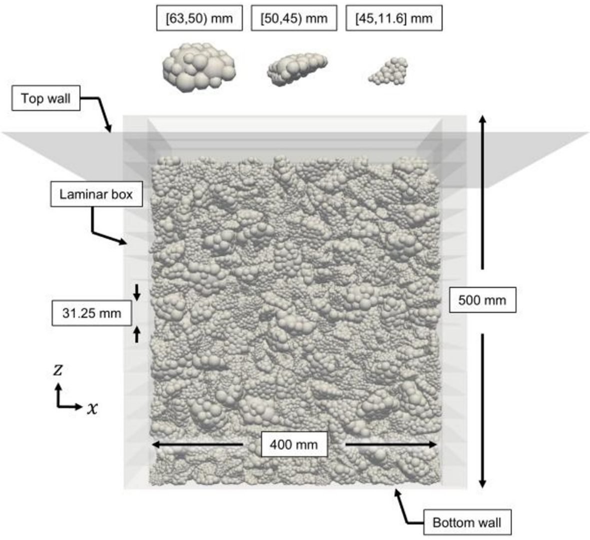

Fig. 1. Discrete element model of the large-scale simple shear setup.

A dry ballast sample with the particle size distribution shown in Fig. 2 was generated within these rigid boundaries by modelling individual ballast particles as clumps of 32 spheres. The density of the individual spheres corresponds to $2900\ \mathrm{kg/m^3}$. The particle size distribution was obtained from sieving new ballast provided by ProRail, the company in charge of the construction and maintenance of the Dutch railway network. It complies with the NEN 13450 standard [9] about the characteristics of the aggregates used for the construction of the upper layer of the railway track. The clumps were created using CLUMP [10] from STL files of laser-scanned particles. Three clump types were defined according to particle size bins (Fig. 1) and scaled to match the target particle size distribution.

The adopted contact law is the Cundall-Strack linear elastic model with Coulomb friction [11]. The input parameters for the different interactions are summarised in Table 1. For the ballast-laminar box frames, ballast-top wall, and ballast-bottom wall interactions, the same Young's modulus and Poisson's ratio as those assigned to the spheres composing the ballast clumps were used to compute the corresponding contact stiffness.

Table 1. Material and interaction parameters for the DEM model using the Cundall-Strack contact model.

Parameter	Value
Poisson's ratio ν [-]	0.2
Young's modulus E [MPa]	40
Friction coefficient ballast-ballast [-]	0.96
Friction coefficient ballast-laminar box [-]	0.35
Friction coefficient ballast-wall [-]	0.96

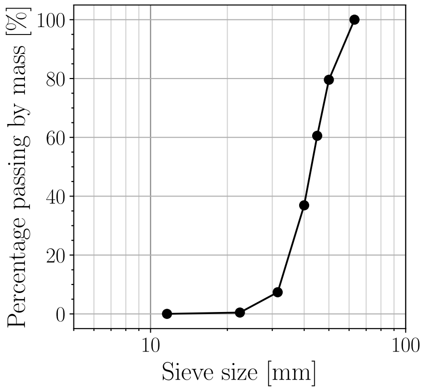

Fig. 2. Particle size distribution of the ballast sample.

These parameters govern the ballast-boundary contact response, whereas the laminar box frames and the top and bottom walls remained kinematically rigid in the DEM model. Interactions between adjacent laminar box frames were not included in the contact detection and force calculation.

Sample preparation consisted of first initializing a cloud of non-interacting clumps, which were then deposited by gravity, to mimic the procedure expected to be followed in the laboratory. Thirteen layers of 10 kg each were sequentially deposited, resulting in a total mass of 130 kg, and a height of approximately 480 mm (the height of 16 stacked frames).

After deposition, the top wall was moved downward until a vertical stress $\sigma_v = 10\ \mathrm{kPa}$ was reached. The vertical stress was calculated from the sum of the vertical forces acting on the top wall divided by the cross-sectional area of the sample ($0.16\ \mathrm{m^2}$).

The initial number of clumps in contact with the top wall, $N_{c,0}$, was 17. As a remark, each clump is composed by several spheres that can potentially interact with the boundary; however, multiple contact points from a single clump are counted as one contact.

To increase the number of contacts, the ballast–ballast, ballast–wall, and ballast–laminar box friction coefficients were set to 0 for particles located within the top 63 mm of the sample (approximately the maximum particle size). Reducing the ballast–ballast friction coefficient allowed the particles near the top boundary to rearrange more freely relative to one another, facilitating the formation of additional contacts with the top wall. This flattening procedure was adopted to control the number of contacts at the top boundary without significantly disturbing the bulk structure of the sample.

During this stage, the top wall maintained a constant vertical stress of 10 kPa by means of an in-built servo-control algorithm implemented in Yade. Four values of $N_{c,0}$ were reached: 32, 76, 103, and 140, which are used to identify the simulations in the following sections. The height of the samples after the compression varied between 440 and 460 mm.

Once the target $N_{c,0}$ was reached, the friction coefficients were restored to their original values, and σ_v was allowed to stabilise at 10 kPa.

Horizontal loading was applied by imposing a velocity gradient across the laminar box frames in the x-direction (displayed in Fig. 1), defined as

$$v_i = v_{bot}\left(\frac{16-i}{16}\right) \tag{1}$$

where $v_{bot} = 0.44\ \mathrm{mm/s}$ is the velocity of the bottom frame, and i is the frame index starting from 0 at the bottom. The frames were displaced towards positive values of x until a shear strain $\gamma = 1.5\%$ was reached and then reversed towards negative values of x until $\gamma = -1.5\%$, completing 10 cycles. The vertical stress was kept constant at 10 kPa.

Throughout the study, the number of contacts with the boundaries during the cyclic loading ($N_{c,top}$ and $N_{c,bot}$) refers to the number of clumps in contact with the respective wall.

3 Macroscopic response

The macroscopic response of the sample is obtained from the horizontal displacement of the laminar box, the vertical displacement of the top plate, and the sum of the horizontal forces acting on the top plate, consistent with the measurements recorded in a laboratory test. These quantities are then interpreted in terms of stresses and strains following the standard approaches used in element testing.

Along with the stress-strain response, the shape of the hysteresis loops can be described by calculating the secant modulus

$$G_{sec} = \frac{\tau_{max}-\tau_{min}}{\gamma_{max}-\gamma_{min}} \tag{2}$$

where γ_{min} and γ_{max} correspond to the minimum and maximum values of shear strain and τ_{min} and τ_{max} to the minimum and maximum values of shear stress, and the damping ratio

$$D = \frac{1}{4\pi}\frac{W_d}{W_s} \tag{3}$$

where W_d is the area enclosed by the hysteresis loop and W_s the area of the triangle defined by the peak coordinates $(\gamma_{max}, \tau_{max})$. To calculate the damping ratio for the open loops, the asymmetric hysteresis loop (ASHL) method by Kumar et al. [12] was used.

3.1 Shear stress, shear strain, and vertical strain

The shear stress-strain τ-γ response of the samples and the evolution of vertical strain ε during the 1st and 10th cycles are shown in Fig. 3. During the 1st cycle clear differences are observed in both the area and the secant stiffness of the hysteresis loops, where both quantities increase with increasing $N_{c,0}$ (Fig. 3a). By the 10th cycle these differences become significantly less pronounced, although the maximum positive shear stress remains higher for the samples with $N_{c,0} \geq 76$ (Fig. 3b).

During the first cycle, the accumulated permanent volumetric strain increases at decreasing $N_{c,0}$ (Fig. 3c), which can be attributed to the greater freedom for rearrangement of particles at the top given the additional space available. By the 10th cycle, the rate at which permanent volumetric strain develops becomes low and similar across all samples (Fig. 3d). The amplitude of the recoverable volumetric strain is calculated as

$$\Delta\varepsilon = \varepsilon_{i,0} - \varepsilon_i \tag{4}$$

where $\varepsilon_{i,0}$ is the accumulated vertical strain at the beginning of the i-th cycle, and ε_i is the accumulated vertical strain at a given point within the cycle. At the 10th cycle, $\Delta\varepsilon$ is also comparable between samples (Fig. 3d).

These results indicate that the number of particles in contact with the top loading cap has a strong influence on the measured response during the initial loading stages. Although this influence decreases as the particle disposition evolves with cycling, a minimum number of contacts is required at the start of the test to obtain a representative response. Therefore, the flattening procedure should also be carefully done in laboratory testing to maximise the number of particles in contact with the top plate.

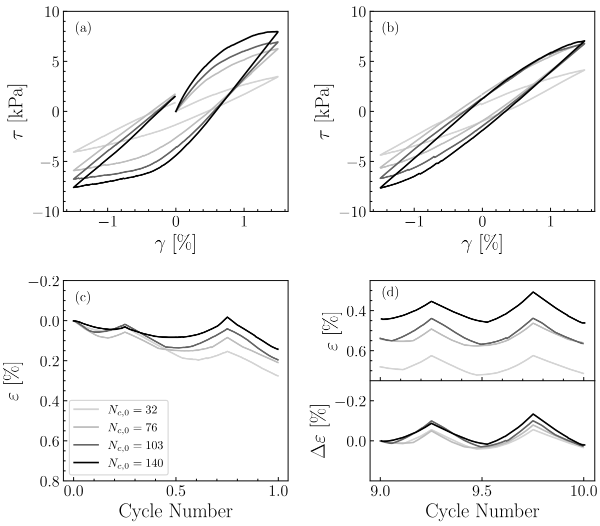

Fig. 3. Shear stress τ vs. shear strain γ for the (a) 1st and (b) 10th cycles of the test, and vertical strain ε vs. cycle number for the (c) 1st and (d) 10th cycles of the tests. $N_{c,0}$ corresponds to the initial number of particles (clumps) in contact with the top wall.

3.2 Secant modulus and damping ratio

The calculated secant shear modulus G_{sec} and damping ratio D for each cycle are presented in Fig. 4. The values of G_{sec}, for an individual sample, remain relatively stable throughout the test, with a relative standard deviation below 5%. However, significant differences are observed between samples with different initial number of contacts.

On average, $G_{sec}$of the sample with $N_{c,0} = 140$ is approximately twice that of the sample with $N_{c,0} = 32$, and the values obtained for the samples with $N_{c,0} = 76$ and $N_{c,0} = 103$ do not converge towards those of the sample with $N_{c,0} = 140$ as the number of cycles increases. Nevertheless, the G_{sec} of the sample with $N_{c,0} = 76$ is only 15% lower than that of the sample with $N_{c,0} = 140$, compared with a reduction of 42% for the sample with $N_{c,0} = 32$.

In contrast, the damping ratio D shows a similar evolution for the samples, especially for those with $N_{c,0} > 32$, decreasing with the number of cycles and converging towards approximately the same value after the 7th cycle.

These results indicate that the secant modulus is more sensitive to the number of particles in contact with the top plate than the damping ratio, suggesting that the energy dissipation mechanisms become less dependent on the initial boundary conditions with cycling.

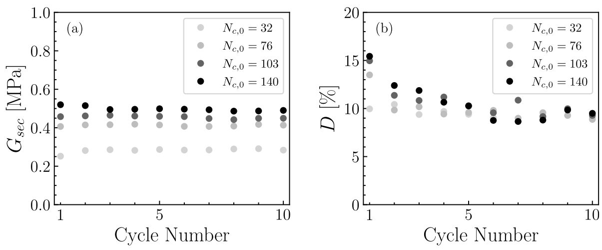

Fig. 4. Evolution of the (a) secant shear modulus G_{sec} and (b) damping D with the number of cycles.

4 Micromechanical investigation

To better understand the differences in the macroscopic response due to the initial number of particles in contact with the top wall, the local response in terms of number of contacts with the boundaries, coordination number, contact force network, and anisotropy of the fabric and force tensors is here discussed.

4.1 Evolution of the number of contacts with the boundaries

The evolution of the number of particles in contact with the top wall ($N_{c,top}$) is shown in Fig. 5a. For samples with $N_{c,0}$ 103 and 140, $N_{c,top}$ decreases during the first cycles and subsequently oscillates around a constant value. For the sample with $N_{c,0} = 76$, $N_{c,top}$ oscillates around approximately 70 contacts from the beginning of the test, with a slight increase after the 4th cycle in the number of contacts when 1.5% of shear strain γ is reached. In contrast, for the sample with $N_{c,0} = 32$, $N_{c,top}$ increases with cycling, and its oscillations are smaller than in the other cases. These results indicate a partial convergence towards a common range of contact numbers at the top boundary, only when the initial configuration has $N_{c,0} \geq 103$.

The number of particles in contact with the bottom boundary remains approximately constant (Fig. 5b), with an average value of about 180 contacts. It is practically not affected by the initial number of contacts at the top wall and does not show a clear dependence on the imposed strain.

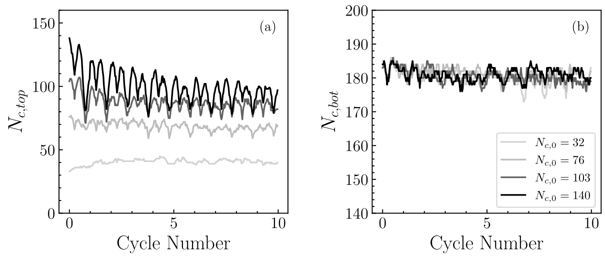

Fig. 5. Evolution of the number of particles in contact with (a) the top wall $N_{c,top}$ and (b) the bottom wall $N_{c,bot}$.

4.2 Coordination number

The coordination number Z is defined as [13]

$$Z = \frac{2C - N_1}{N - N_0 - N_1} \tag{5}$$

where C is the total number of contacts, N is the total number of particles, and N_1 and N_0 are the number of particles with only one or no contacts, respectively. It is worth highlighting that contacts are counted at the particle level. Therefore, when two particles interact at multiple contact points, they are considered to form a single contact for the purpose of computing C.

To assess spatial variations, the sample was divided into horizontal layers with a thickness of 20% the total specimen height, and Z was computed within each layer (Fig. 6). The vertical position of the layers is expressed using relative heights h_{rel} defined as

$$h_{rel} = \frac{z}{H} \tag{6}$$

where z is the vertical coordinate ($z = 0$ at the bottom of the laminar box) and H is the total sample height.

In the topmost region (h_{rel} = 0.8-1), where the flattening procedure was applied, Z markedly decreases during the first four cycles, especially for larger $N_{c,0}$. This reduction reaches an asymptotic value after approximately four cycles, being the asymptotic value larger for larger $N_{c,0}$.

In the underlying slab (h_{rel} = 0.6-0.8), Z shows a slight decrease during the initial cycles. For samples with $N_{c,0} \geq 76$ it stabilizes and oscillates around approximately the same value, whereas the sample with $N_{c,0} = 32$ oscillates around a slightly higher value.

For the two intermediate slabs (h_{rel} = 0.2-0.6), the amplitude of the oscillations decreases, and all samples exhibit similar values of Z, indicating a reduced influence of the top boundary condition. Within this portion of the sample more representative measurements of the material behaviour may be taken.

Finally, in the bottom slab, all samples again oscillate around a common mean value, however, the oscillation amplitude is the largest between all layers, suggesting an influence of the bottom boundary in the response of the material.

Overall, after the first cycle, the coordination number increases with depth, due to the higher confinement induced by the weight of the overlying material.

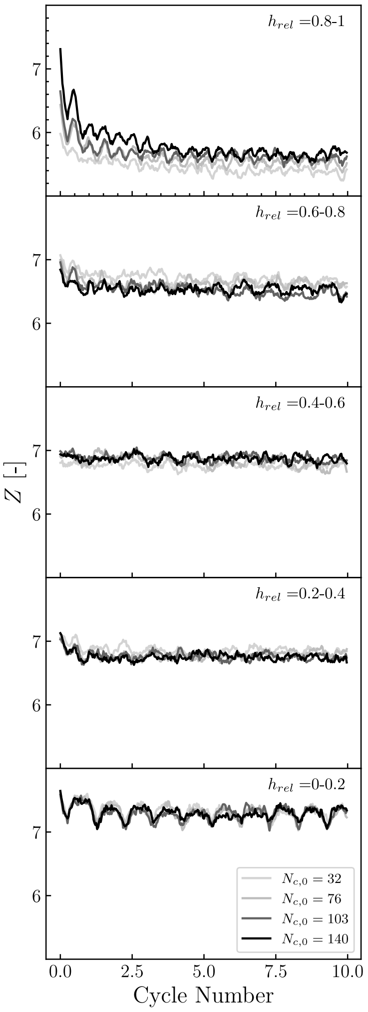

Fig. 6. Evolution of the coordination number Z inside different layers.

4.3 Contact force network

The contact force network at $\gamma = 1.5\%$ during the 1st cycle is shown in Fig. 7 for the sample with $N_{c,0} = 32$ and in Fig. 8 for the sample with $N_{c,0} = 140$. The force network was divided into contacts with normal forces greater than the mean (Fig. 7a and Fig. 8a), and lower than the mean (Fig. 7b and Fig. 8b), representing the strong and weak force networks. In the strong network, the darkest colour corresponds to forces equal to or greater than the 95th percentile.

Both samples display a similar structure in the weak force network, with no clear localization of force magnitudes or preferential orientation. This behaviour continues throughout all loading cycles.

In contrast, the strong force network develops a preferential direction. For the sample with $N_{c,0} = 32$, lower force magnitudes are observed in the top-left region of the specimen (Fig. 7a), in the area where fewer particles are in contact with the top wall. This suggests that, in this region, force transmission is primarily carried by one side of the sample, while the other side remains largely unloaded.

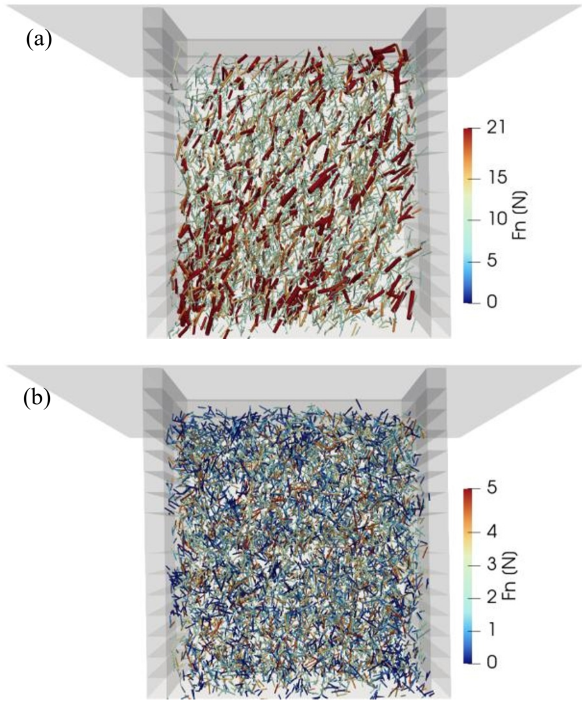

Fig. 7. (a) Strong and (b) weak normal force F_n contact network at a shear strain of 1.5% during the first cycle. Sample with $N_{c,0} = 32$.

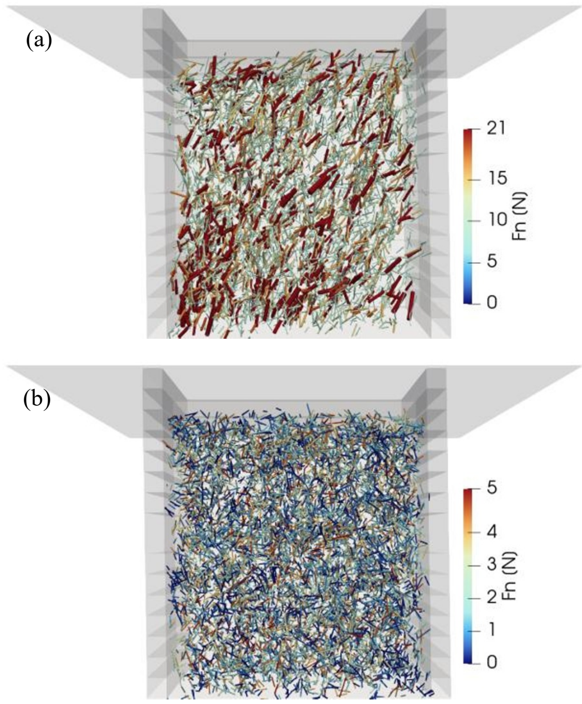

Fig. 8. (a) Strong and (b) weak normal force F_n contact network at a shear strain of 1.5% during the first cycle. Sample with $N_{c,0} = 140$.

At $\gamma = 1.5\%$ during the 10th cycle (Fig. 9), force bands are evident in both samples. These bands are thicker for the sample with $N_{c,0} = 140$, particularly in the upper third of the sample.

These observations indicate that boundary conditions primarily influence the structure of the strong force network. In particular, a lower number of contacts at the top boundary causes localized reductions in force transmission, such that only a part of the top wall effectively transmits load. As a result, the stress distribution within the sample becomes non-uniform, with regions that remain largely unloaded. In contrast, a higher number of contacts promotes a more distributed load transfer and wider strong force chains.

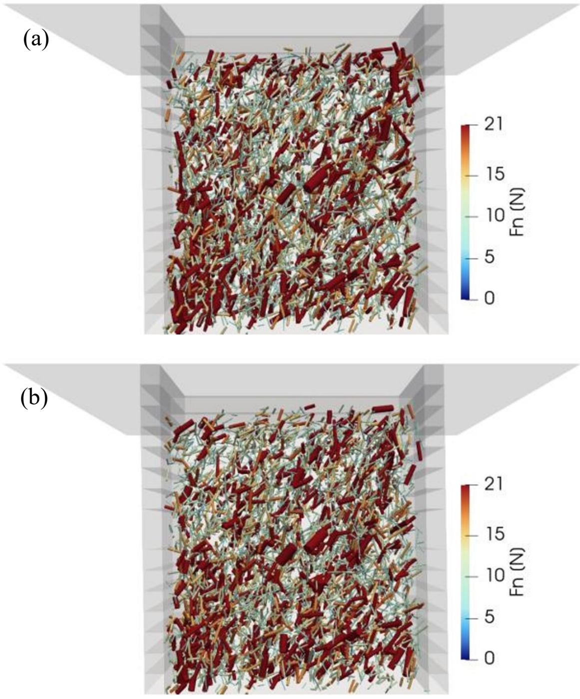

Fig. 9. Strong normal force F_n contact network at a shear strain of 1.5% during the 10th cycle for (a) sample with $N_{c,0} = 32$ and (b) sample with $N_{c,0} = 140$.

4.4 Anisotropy of the fabric

The components Φ_{ij} of the fabric tensor $\boldsymbol{\Phi}$ are calculated from the components of the contact normal vectors $\boldsymbol{n}$ as [14]

$$\Phi_{ij} = \frac{1}{C}\sum_{k=1}^{C} n_i^k n_j^k \qquad (7)$$

where C is the total number of contacts, as in Equation (3).

Using the eigenvalues of the tensor $\Phi_1 \geq \Phi_2 \geq \Phi_3$, anisotropy descriptors $\beta_{1,\Phi}$ and $\beta_{2,\Phi}$ can be calculated as [15]

$$\beta_{1,\Phi} = \ln\left(\frac{\Phi_1}{\Phi_3}\right) \qquad (8)$$

and

$$\beta_{2,\Phi} = \ln\left(\frac{\Phi_1}{\Phi_2}\right)\Big/\ln\left(\frac{\Phi_2}{\Phi_3}\right) \qquad (9)$$

The parameter $\beta_{1,\Phi}$ provides a measure of the intensity of the anisotropy, increasing as contact normals become preferentially aligned a dominant direction. The first anisotropy descriptor $\beta_{1,\Phi}$ was presented as a logarithmic ratio by Woodcock [15] to compare distributions with eigenvalue ratios of different orders of magnitude.

The parameter $\beta_{2,\Phi}$ characterises the shape of the orientation distribution. Values of $\beta_{2,\Phi} > 1$ indicate a clustered distribution, where contact normals concentrate around a single preferred direction. On the other hand, when $\beta_{2,\Phi} < 1$, the contact normals are predominantly distributed within a plane (i.e., forming a ring on the unit sphere).

Similarly to $\beta_{1,\Phi}$, $\beta_{2,\Phi}$ is presented as a ratio of logarithms to easily describe the distribution shape using two and three-axis plots [15].

In addition, the angle θ_Φ, defined as the angle between the major principal fabric eigenvector projected onto the XZ plane and the x-axis, is used to describe the mean orientation of the contact network. A value of $\theta_\Phi = 90°$ indicates that contact normals are predominantly aligned in the vertical direction, values lower than 90° indicate a preferential orientation towards positive values of x, while values greater than 90° towards negative values of x.

The values of $\beta_{1,\phi}$ (Fig. 10a) show that the overall intensity of fabric anisotropy is low for all samples, its average value decreases with increasing number of cycles, and it decreases with increasing $N_{c,0}$. For all samples, the intensity of anisotropy reaches its (local) maximum at $|\gamma| = 1.5\%$, and its (local) minimum at $\gamma = 0\%$.

The values of $\beta_{2,\Phi}$ (Fig. 10b) indicate that contact normals tend to arrange in clusters, and that the degree of clustering is highest at $\gamma = 0\%$. The sample with $N_{c,0} = 32$ shows the strongest tendency towards clustering of contact normals, as its values of $\beta_{2,\Phi}$ are the highest among the four samples.

The mean orientation of the contact normals is similar for all samples and evolves in phase with the applied loading (Fig. 10c). Specifically, θ_Φ reaches its minimum at $\gamma = 1.5\%$ and its maximum at $\gamma = -1.5\%$.

These results indicate that the initial contact configuration affects the intensity of the fabric anisotropy during the first cycles, and the degree of clustering for the sample with $N_{c,0} = 32$, and that the evolution of fabric is primarily controlled by the cyclic loading conditions.

4.5 Anisotropy of the force

Similar to the fabric tensor, the components f_{ij} of the force tensor $\boldsymbol{f}$, are calculated as [2]

$$f_{ij} = \frac{1}{C}\sum_{k=1}^{C} f_i^k f_j^k \qquad (10)$$

where f^k is the unit contact force, and C is the total number of contacts, as in Equation (3). Chen et al. [2] use the same eigenvalue approach as for the fabric tensor, and calculate anisotropy descriptors $\beta_{1,f}$ and $\beta_{2,f}$ as

$$\beta_{1,f} = \ln\left(\frac{f_1}{f_3}\right) \tag{11}$$

and

$$\beta_{2,f} = \ln\left(\frac{f_1}{f_2}\right) \Big/ \ln\left(\frac{f_2}{f_3}\right) \tag{12}$$

where $f_1 \geq f_2 \geq f_3$ are the eigenvalues of the tensor.

The angle between the major principal unit force eigenvector projected onto the XZ plane and the x-axis θ_f, similar to θ_Φ, is used to describe the mean orientation of the force network.

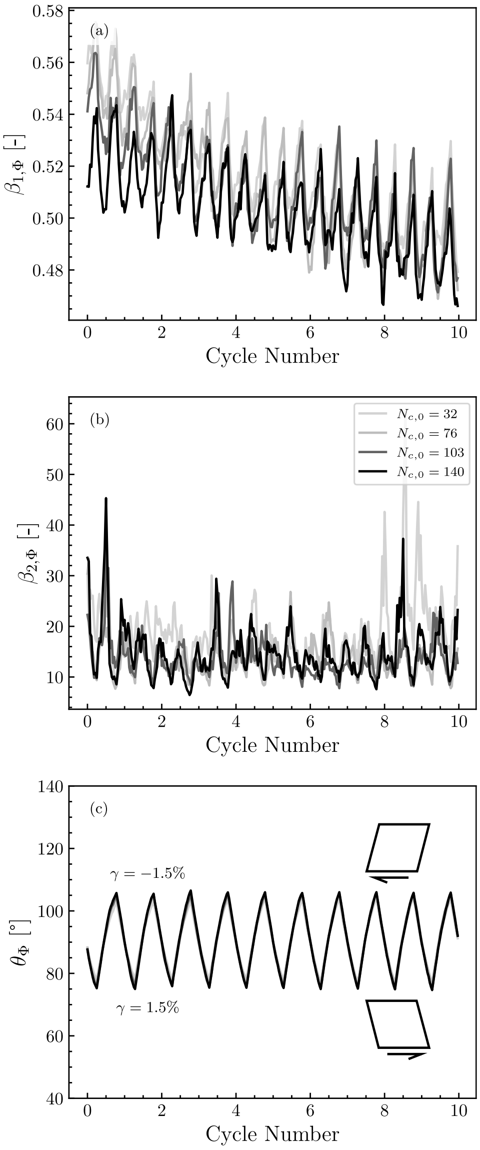

Fig. 10. Evolution of (a) the fabric anisotropy degree $\beta_{1,\Phi}$, (b) the fabric anisotropy geometry $\beta_{2,\Phi}$, and (c) the major principal fabric orientation θ_Φ.

During a single cycle, the intensity of unit contact force anisotropy $\beta_{1,f}$ is similar for samples with $N_{c,0} \geq 76$ (Fig. 11a) and is, on average, higher than that of the sample with $N_{c,0} = 32$. The evolution of $\beta_{1,f}$ for the unit force tensor exhibits a period equal to that of the loading cycle, whereas $\beta_{1,\Phi}$ varies twice within a cycle. As a result, $\beta_{1,f}$ reaches its maximum at $\gamma = 1.5\%$, and its minimum at $\gamma = -1.5\%$, which is consistent with the lower shear stresses reached at $\gamma = -1.5\%$ (Section 3).

The values of $\beta_{2,f}$ (Fig. 11b) are approximately one order of magnitude lower than those of the fabric tensor, indicating that the unit force vectors are less clustered. This effect is particularly evident at $\gamma = -1.5\%$ where $\beta_{2,f}$ reaches its minimum.

The major orientation angle θ_f of the unit force tensor is similar for all samples (Fig. 11c), consistently with that of the fabric tensor. However, unlike the fabric tensor, θ_f does not oscillate around 90°, indicating that the force network does not fully reorient with the cyclic reversal of the loading direction.

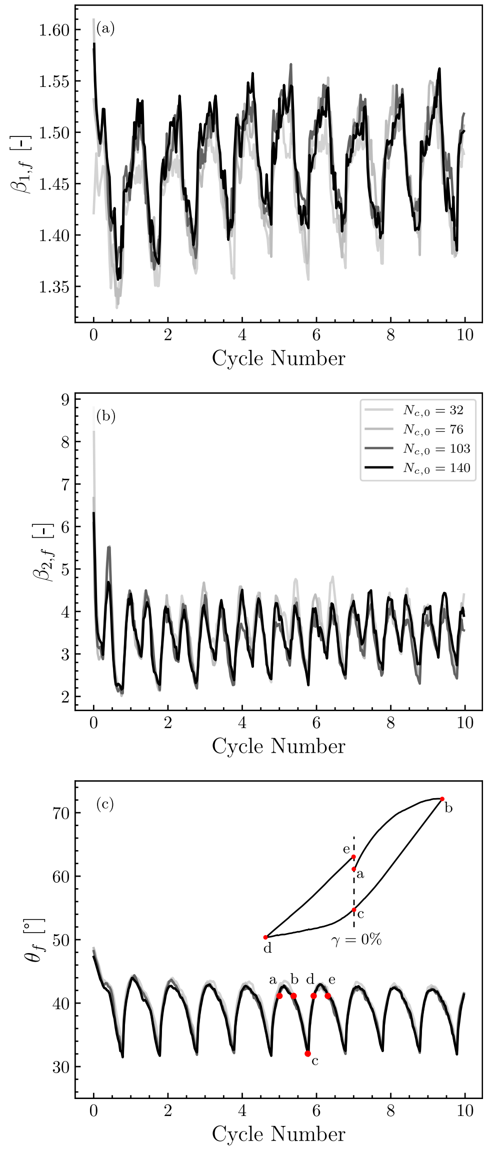

Fig. 11. Evolution of (a) the force anisotropy degree β_1, (b) the force anisotropy geometry β_2, and (c) the major principal force orientation θ.

The results show that the unit force anisotropy is systematically higher than the fabric anisotropy, thus the forces are more directional than the contact network itself.

In addition, the lower values of $\beta_{2,f}$ compared to $\beta_{2,\Phi}$ suggest that, although contact normals tend to cluster, the forces are distributed over a broader set of directions, forming a more diffuse network. Finally, the force network is more directionally concentrated than the contact network, and θ_f exhibits reduced symmetry than θ_Φ with respect to the input loading.

5 Conclusions

A cyclic shear test on a ballast sample was replicated using DEM simulations. The aim of the numerical analysis was to unravel and assess the influence of the number of particles in contact with the top loading cap on the macroscopic and micromechanical response of the sample. The results highlight the importance of ensuring a sufficient number of contacts at the loading boundary both in numerical simulations and in experimental testing.

The results show that the number of contacts at the top boundary has a strong influence on the measured macroscopic response during the initial loading stages, if the initial number of contacts at the top boundary remains smaller than approximately 50% of the maximum achievable number of contacts. Differences in shear and volumetric response are most pronounced during the first cycles and progressively diminish as the material structure evolves. However, full convergence is not observed for all macroscopic quantities. The secant shear modulus remains particularly sensitive to the initial number of top boundary contacts, whereas the damping ratio becomes less dependent on the initial contact configuration over cycling. The influence of the initial contact configuration on the coordination number is confined to the upper region of the sample, with the central and lower parts of the specimen showing comparable values across all simulations.

Micromechanical analyses show that the boundary conditions primarily affect the structure of the strong force network. A low number of contacts at the top boundary leads to localized and non-uniform force transmission, with portions of the sample remaining largely unloaded, whereas higher numbers of contacts promote a more homogeneous distribution of strong force chains. In contrast, the weak force network remains largely isotropic. The fabric tensor shows low anisotropy, with the intensity of the anisotropy varying between samples during the initial cycles and the shape of the distribution of contact normals indicating a more planar arrangement for the sample with the lowest number of contacts. The fabric orientation rotates with the loading direction.

In contrast, the unit force tensor exhibits higher anisotropy but a more consistent evolution across samples, with both the intensity and shape of the distribution of unit force vectors remaining largely unaffected by the initial number of contacts. Unlike the fabric, the orientation of the force network remains biased towards one direction, indicating a directional memory in force transmission.

The work is part of the research project STEM. The authors acknowledge the financial support of ProRail, NL.

References

1. Q. Gu, C. Zhao, X. Bian, J. P. Morrissey, J. Y. Ooi, Trackbed settlement and associated ballast degradation due to repeated train moving loads, Soil Dyn. Earthq. Eng., **153**, 107109 (2022). https://doi.org/10.1016/j.soildyn.2021.107109
2. J. Chen, B. Indraratna, J. S. Vinod et al., Stress–dilatancy behaviour of fouled ballast: experiments and DEM modelling, Granul. Matter, **23**, 90 (2021). https://doi.org/10.1007/s10035-021-01150-1
3. S. Lenart, A. M. Kaynia, Dynamic properties of lightweight foamed glass and their effect on railway vibration, Transp. Geotech., **21**, 100276 (2019). https://doi.org/10.1016/j.trgeo.2019.100276
4. S. Lenart, S. R. Karumanchi, Deformation properties and performance evaluation of reused ballast with waste tire-derived aggregates, Transp. Geotech., **52**, 101586 (2025). https://doi.org/10.1016/j.trgeo.2025.101586
5. D.-S. Xu, H.-B. Liu, R. Rui, Y. Gao, Cyclic and postcyclic simple shear behavior of binary sand–gravel mixtures with various gravel contents, Soil Dyn. Earthq. Eng., **123**, 230–241 (2019). https://doi.org/10.1016/j.soildyn.2019.04.030
6. W. Jia, V. Markine, Y. Guo, G. Jing, Experimental and numerical investigations on the shear behaviour of recycled railway ballast, Constr. Build. Mater., **217**, 310–320 (2019). https://doi.org/10.1016/j.conbuildmat.2019.05.020
7. A. S. J. Suiker, E. T. Selig, R. Frenkel, Static and cyclic triaxial testing of ballast and subballast, J. Geotech. Geoenviron. Eng., **131**, 771–782 (2005). https://doi.org/10.1061/(ASCE)1090-0241(2005)131:6(771)
8. V. Angelidakis, K. Boschi, K. Brzeziński et al., YADE – an extensible framework for the interactive simulation of multiscale, multiphase, and multiphysics particulate systems, Comput. Phys. Commun., **304**, 109293 (2024). https://doi.org/10.1016/j.cpc.2024.109293
9. NEN-EN 13450:2003+C1:2006, Toeslagmaterialen voor spoorwegballast. https://www.nen.nl/nen-en-13450-2003-c1-2006-nl-128804
10. V. Angelidakis, S. Nadimi, M. Otsubo, S. Utili, CLUMP: a code library to generate universal multi-sphere particles, SoftwareX, **15**, 100735 (2021). https://doi.org/10.1016/j.softx.2021.100735
11. P. A. Cundall, O. D. L. Strack, A discrete numerical model for granular assemblies, Géotechnique, **29**, 47–65 (1979). https://doi.org/10.1680/geot.1979.29.1.47
12. S. S. Kumar, A. M. Krishna, A. Dey, Evaluation of dynamic properties of sandy soil at high cyclic strains, Soil Dyn. Earthq. Eng., **99**, 157–167 (2017). https://doi.org/10.1016/j.soildyn.2017.05.016
13. C. Thornton, Numerical simulations of deviatoric shear deformation of granular media, Géotechnique, **50**, 43–53 (2000). https://doi.org/10.1680/geot.2000.50.1.43
14. A. E. Scheidegger, On the statistics of the orientation of bedding planes, grain axes, and similar sedimentological data, USGS PP, **525**.C, 164-167 (1963). https://pubs.usgs.gov/pp/0525c/report.pdf
15. N. H. Woodcock, Specification of fabric shapes using an eigenvalue method, GSA bulletin, **88** (9), 1231-1236 (1977). https://doi.org/10.1130/0016-7606(1977)88<1231:SOFSUA>2.0.CO;2